Mathematics

AIMS Mathematics, 11(3): 5669–5691.
DOI: 10.3934/math.2026233
Received: 11 October 2025
Revised: 14 January 2026
Accepted: 26 February 2026
Published: 05 March 2026

https://www.aimspress.com/journal/Math

Research article

Groundwater flow in a two-region aquifer: A 2D analytical solution with recharge forcing

Ming-Chang Wu[1] and Ping-Cheng Hsieh[2,*]

[1] National Yunlin University of Science and Technology-Research Center for Soil & Water Resources and Natural Disaster Prevention, Douliu, Yunlin County, Taiwan
[2] Department of Soil and Water Conservation, National Chung Hsing University, Taichung 40227, Taiwan

* **Correspondence:** Email: ida364@email.nchu.edu.tw; Tel: +8860422840381; Fax: +8860422840381.

Abstract: Aquifer systems are often simplified as homogeneous and infinite, yet natural deposits typically display heterogeneity and occur within finite domains. In this study, we developed a two-dimensional analytical framework for groundwater flow in an unconfined two-region aquifer that represents lateral heterogeneity through piecewise hydraulic properties, subjected to spatially variable recharge, formulated using the generalized integral transform technique (GITT). The model was benchmarked against finite-difference simulations of the nonlinear Boussinesq equation, showing close agreement and validating the linearized approach. Applications to contrasting soil properties and recharge patterns revealed that heterogeneity and recharge variability strongly influence groundwater levels and hydraulic gradients. Uniform recharge leads to higher mounding in low-permeability zones, while spatially increasing recharge amplifies head buildup and steepens gradients. In contrast, decreasing recharge shifts the mound toward the aquifer center and produces outward flow. Comparisons between homogeneous and two-region composite aquifers showed that only the latter exhibit abrupt head changes at interfaces. The framework provides a practical tool for groundwater analysis and management.

Keywords: groundwater flow; heterogeneity; recharge; 2D analytical model; Boussinesq equation
Mathematics Subject Classification: 76S05

1. Introduction

Unconfined aquifers are typically formed through fluvial and alluvial processes, producing layered deposits with varied sedimentary facies. These depositional patterns create substantial contrasts in hydraulic conductivity, specific yield, and directional anisotropy (Montalto et al. [1]). In Taiwan's Zhuoshui River basin, for example, clay and silt layers with low permeability have accumulated into an alluvial fan that strongly influences regional groundwater dynamics. Such heterogeneity in subsurface materials plays a decisive role in groundwater storage and movement. Heterogeneous conditions are also common in coastal aquifers (Li et al. [2]; Li et al. [3]; Xia and Li [4]; Kreyns et al. [5]), where spatial variability in hydraulic conductivity $K(x)$ and recharge distribution $r(x)$ controls changes in groundwater head $h(x,t)$. Understanding how these parameters interact is essential for groundwater management, contaminant transport assessment, and recharge estimation. Numerous investigations have demonstrated that incorporating heterogeneity leads to more realistic models. For instance, Winter and Tartakovsky [6] developed a stochastic composite-aquifer framework that produced more accurate hydraulic head predictions. Kalbus et al. [7] showed that including heterogeneity in aquifers and streambeds improved simulated flux distributions. Similarly, Illman et al. [8] validated heterogeneous aquifer models with pumping tests and sandbox experiments, reporting improved prediction accuracy when heterogeneous conductivity fields were incorporated. Hartmann et al. [9] further emphasized that geological variability strongly governs water balance, and that ignoring recharge variability limits the usefulness of analytical solutions.

Despite these insights, deriving analytical expressions for heterogeneous aquifers remains challenging. Serrano [10] applied decomposition methods to address the nonlinear Boussinesq equation, revealing that linearized and nonlinear formulations differ greatly under high gradients, strong recharge, or low hydraulic conductivity. Moreover, researchers have approximated heterogeneity by substituting aquifers with finite or piecewise homogeneous regions. For example, Trefry [11] examined flow through layered aquifers subject to sinusoidal boundaries. Chuang et al. [12] modeled leaky aquifers subdivided into horizontal regions, and Ptak et al. [13] reviewed tracer testing as a tool for parameter characterization in heterogeneous porous media.

Advances have leveraged the generalized integral transform technique (GITT) to tackle one-dimensional groundwater problems. Wu and Hsieh [14] demonstrated its rapid convergence relative to Laplace transform solutions and analyzed aquifer behavior under different recharge conditions. Classical treatments of separation of variables and multilayer media (Morse and Feshbach [15]; Özisik [16]) highlight practical barriers to deriving eigenvalues/eigenfunctions as system complexity grows (Mulholla and Cobble [17]; Sun and Wichman [18]); and researchers have estimated conductivity, source/sink terms, and boundary conditions directly from field constraints (Zhang [19]). Semi-analytical developments have also entailed transient recharge and aquifer heterogeneity in two dimensions (Das et al. [20]), and researchers assessed recharge estimation errors under anisotropy and heterogeneous hydraulic conductivity K (Águila et al. [21]). Hemker and Bakker [22] developed analytical solutions for steady groundwater flow in a heterogeneous, anisotropic, semiconfined aquifer composed of multiple horizontal layers, each subdivided into homogeneous cells with distinct hydraulic conductivity tensors. Their multilayer analytical framework demonstrated that when the major principal direction of the transmissivity tensor varies between layers, streamlines may become spiral-shaped, forming organized bundles termed "groundwater whirls". Guo et al. [23] derived analytical solutions describing tide-induced groundwater head fluctuations in a two-zone system

consisting of a finite-width coastal zone connected to an inland zone of contrasting properties. They introduced a dimensionless zone-contrast parameter governed by the ratio of the transmissivity–storativity products between the inland and coastal zones, and showed that this lateral contrast controls amplitude attenuation and phase propagation across zones; they also discussed implications for inverse estimation of aquifer parameters and demonstrated application to a field case in China. In river–aquifer systems with transient forcing, Liang and Zhang [24] presented 1D analytical solutions for the water table and lateral discharge in a heterogeneous unconfined aquifer subject to time-dependent sources while being bounded by a fluctuating river stage, with heterogeneity represented by multiple sections of differing hydraulic conductivity.

Building on this literature, Wu and Hsieh [25] provided a full analytical description of 1D unconfined sloping aquifers under general spatiotemporal recharge, overcoming the quasi-steady assumptions of prior formulations. Hsieh and Wu [26] later integrated perturbation methods with GITT to examine river-aquifer interactions, adjusting recharge via Horton's law and validating with field evidence. Motivated by these advances and persisting gaps, we develop a two-dimensional analytical solution for groundwater flow in a horizontal two-region unconfined aquifer under spatially distributed recharge. The formulation is benchmarked against nonlinear finite-difference simulations and then applied to explore how heterogeneity and recharge distribution together shape groundwater levels and flow discharges.

2. Materials and methods

2.1. Analytical formulation

Unconfined flow is formulated here with a Boussinesq-type relation—Darcy flux coupled with mass conservation under the Dupuit–Forchheimer approximation. Rather than presuming a uniform medium, the aquifer is represented as two adjacent vertical zones (regions I and II) separated at $x = L_m$ (Figure 1). The aquifer domain $L_x \times L_y \times D$ enables each zone to carry its own hydraulic properties, reflecting realistic lateral heterogeneity.

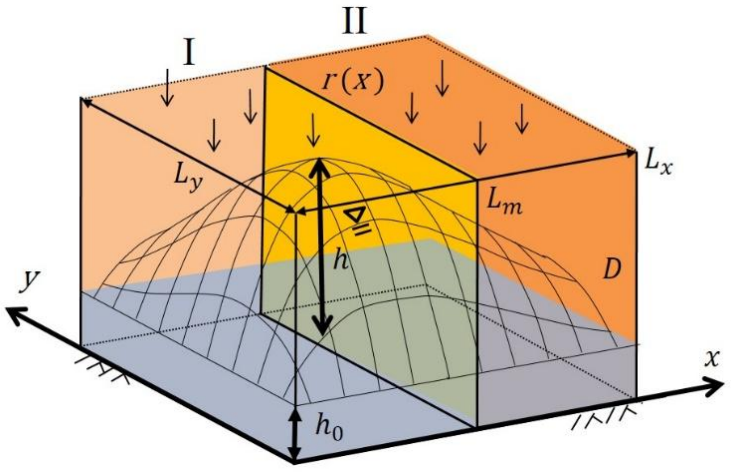

Figure 1. Conceptual diagram of a horizontal two-region unconfined aquifer, with surface recharge applied across the domain.

According to Darcy's law, the unit-width discharge components in the horizontal directions are:

$$q_x = -K_x h \frac{\partial h}{\partial x} \tag{1}$$

$$q_y = -K_y h \frac{\partial h}{\partial y} \tag{2}$$

where K_x and K_y are the hydraulic conductivities along the x and y axes, respectively, and $h \equiv h(x, y, t)$ is the saturated thickness. Conservation of mass requires:

$$S_y \frac{\partial h}{\partial t} + \frac{\partial q_x}{\partial x} + \frac{\partial q_y}{\partial y} = r \tag{3}$$

where S_y denotes specific yield, and $r \equiv r(x, y)$ represents recharge (per unit area, per unit time). t is time.

For a two-region aquifer, the governing two-dimensional Boussinesq equations with a space-dependent source term $r(x)$ or $r(x, y)$ for the two regions are:

$$S_{y,1} \frac{\partial h}{\partial t} - K_{1,x} \frac{\partial}{\partial x}\left(h \frac{\partial h}{\partial x}\right) - K_{1,y} \frac{\partial}{\partial y}\left(h \frac{\partial h}{\partial y}\right) = r(x, y), 0 < x < L_m, 0 < y < L_y \tag{4}$$

$$S_{y,2} \frac{\partial h}{\partial t} - K_{2,x} \frac{\partial}{\partial x}\left(h \frac{\partial h}{\partial x}\right) - K_{2,y} \frac{\partial}{\partial y}\left(h \frac{\partial h}{\partial y}\right) = r(x, y), L_m < x < L_x, 0 < y < L_y \tag{5}$$

subject to the following conditions:

- Initial water level: uniform initial water table

$$h(x, y, 0) = h_0, 0 < x < L_x, 0 < y < L_y. \tag{6}$$

- Constant head at $x = 0$:

$$h(0, y, t) = h_0, 0 < y < L_y, t > 0 \tag{7}$$

  representing hydraulically controlled boundaries (e.g., river/constant-head boundary segments or reference head boundaries).

- Interface continuity conditions at $x = L_m$: continuity of head and continuity of flux across the material boundary, ensuring mass conservation across the two regions

$$h(x = L_m{}^-) = h\left(x = L_m{}^+\right), 0 < y < L_y, t > 0, \tag{8}$$

$$K_{1,x} \frac{\partial h(x = L_m{}^-)}{\partial x} = K_{2,x} \frac{\partial h\left(x = L_m{}^+\right)}{\partial x}, 0 < y < L_y, t > 0. \tag{9}$$

- No-flow boundaries at $x = L_x$ and $x = L_y$:

$$\frac{\partial h}{\partial x} = 0, x = L_x, 0 < y < L_y, t > 0 \tag{10}$$

$$\frac{\partial h}{\partial y} = 0, 0 < x < L_x, y = L_y, t > 0 \tag{11}$$

representing groundwater divides/symmetry or impermeable boundaries at the domain edges.

- Constant head at $y = 0$:

$$h = h_0, 0 < x < L_x, y = 0, t > 0 \tag{12}$$

where $K_{i,x}$ and $K_{i,y}$ $(i = 1, 2)$ are hydraulic conductivities of region i in the x and y directions, respectively; $S_{y,i}$ is specific yield of region i; and h_0 is the initial water table.

These boundary choices define the domain's drainage pathways and symmetry constraints, which shape mound location and discharge patterns; therefore, the current solution is best interpreted as an analytical benchmark for a rectangular domain with mixed Dirichlet–Neumann boundaries. Other alternative boundary types (e.g., specified flux and mixed boundaries) would require modified eigenfunctions and are outside the scope of this study.

The recharge is a temporally uniform and spatially piecewise uniform distribution:

$$r(x, y) = \sum_{i=1}^{M} [u(x - x_{i-1}) - u(x - x_i)]\,[u(y - y_0) - u(y - y_1)] \tag{13}$$

where u(-) denotes the unit step function; M denotes the total number of increments along x; and $[y_0,\ y_1]$ defines the recharge interval in the y direction. In this study, $y_0 = 0$ and $y_1 = L_y$.

2.2. Linearization and nondimensionalization

The nonlinearity in Eqs (4) and (5) generally precludes closed-form solutions. Classical approaches often approximate either the groundwater head h or the squared head h^2 term (Bear [27]). Following prior guidance that linearizing the squared head h^2 yields better fidelity than linearizing h (Guo [28]; Liang and Zhang ([29,30]), we adopt that approach and then recast the problem in dimensionless form (Guo [28]; Serrano [10]; Gao et al. [31]). This produces the coupled linear boundary-value problems (14)–(22) used throughout. Using the scalings

$$H = \left(h^2 - {h_0}^2\right)/{h_0}^2,\ X = x/L_x,\ Y = y/L_y,\ T = t/t_d,\ R = rt_d/h_0$$

with anisotropy ratios given by $K_{i,r} = K_{i,y}/K_{i,x}$ $(i = 1, 2)$ and t_d representing the recharge period, this leads directly to (14)–(22):

$$\frac{\partial^2 H}{\partial X^2} + p_1 \frac{\partial^2 H}{\partial Y^2} + \gamma_1 R(X, Y) = \tau_1 \frac{\partial H}{\partial T}, 0 < X < L_m/L_x, 0 < Y < 1 \tag{14}$$

$$\frac{\partial^2 H}{\partial X^2} + p_2 \frac{\partial^2 H}{\partial Y^2} + \gamma_2 R(X, Y) = \tau_2 \frac{\partial H}{\partial T}, L_m/L_x < X < 1, 0 < Y < 1 \tag{15}$$

$$H = 0, 0 < X < 1, 0 < Y < 1, T = 0 \tag{16}$$

$$H = 0, X = 0, Y > 0, T > 0 \tag{17}$$

$$H(X = L_m/{L_x}^-) = H\left(X = L_m/{L_x}^+\right), 0 < Y < 1, T > 0 \tag{18}$$

$$K_{1,x} \frac{\partial H(X = L_m/{L_x}^-)}{\partial X} = K_{2,x} \frac{\partial H\left(X = L_m/{L_x}^+\right)}{\partial X}, 0 < Y < 1, T > 0 \tag{19}$$

$$\frac{\partial H}{\partial X} = 0, X = 1, 0 < Y < 1, T > 0 \tag{20}$$

$$H = 0, 0 < X < 1, Y = 0, T > 0 \tag{21}$$

$$\frac{\partial H}{\partial Y} = 0, 0 < X < 1, Y = 1, T > 0 \tag{22}$$

where

$$p_i = K_{i,r}\frac{{L_x}^2}{{L_y}^2},\ \gamma_i = \frac{{L_x}^2}{K_{i,x}t_d h_0},\ \tau_i = \frac{S_{y,i}{L_x}^2}{K_{i,x}t_d h_0} \quad (i = 1, 2).$$

The boundary conditions are homogeneous and correspond to constant head at $X = 0$, no-flow at $X = 1$, and symmetry at $Y = 0, 1$.

2.3. Eigenfunction expansion

To construct analytical solutions for the two-region system, the separation-of-variables technique is applied. The dimensionless groundwater head is expressed as a separable product of spatial and temporal components:

$$H(X, Y, T) = \phi(X)\psi(Y)\Gamma(T). \tag{23}$$

This representation is consistent with the linearized heterogeneous formulation introduced in Section 2.2. Substituting (23) into the governing boundary-value problems (14)–(15) for regions I and II yields two eigenvalue problems. Each system consists of a Helmholtz-type equation in X with eigenvalue α, a scaled Helmholtz form in Y with eigenvalue β, and a first-order temporal ODE at a decay rate depending on α^2, β^2, and τ_i:
For $0 \le X \le L_m/L_x$:

$$\begin{cases} \dfrac{d^2\phi}{dX^2} + \alpha^2\phi = 0 \\ p_1\dfrac{d^2\psi}{dY^2} + \beta^2\psi = 0 \\ \tau_1\dfrac{d\Gamma}{dT} + (\alpha^2 - \beta^2)\Gamma = 0 \end{cases}$$

$$\begin{cases} \frac{d^2\phi}{dX^2} + \alpha^2\phi = 0 \\ p_1\frac{d^2\psi}{dY^2} + \beta^2\psi = 0 \\ \tau_1\frac{d\Gamma}{dT} + (\alpha^2 - \beta^2)\Gamma = 0 \end{cases}. \tag{24}$$

For $L_m/L_x \le X \le 1$:

$$\begin{cases} \frac{d^2\phi}{dX^2} + \alpha^2\phi = 0 \\ p_2\frac{d^2\psi}{dY^2} + \beta^2\psi = 0 \\ \tau_2\frac{d\Gamma}{dT} + (\alpha^2 - \beta^2)\Gamma = 0 \end{cases}. \tag{25}$$

The associated boundary and interface conditions are:

$$\phi(0) = 0 \tag{26}$$

$$\phi(L_m/L_x^-) = \phi\left(L_m/L_x^+\right) \tag{27}$$

$$K_{1,x}\frac{d\phi(L_m/L_x^-)}{dX} = K_{2,x}\frac{d\phi\left(L_m/L_x^+\right)}{dX} \tag{28}$$

$$\frac{d\phi}{dX}(1) = 0 \tag{29}$$

$$\psi(0) = 0 \tag{30}$$

$$\frac{d\psi}{dY}(1) = 0. \tag{31}$$

Equations (24)–(31) pose a complete eigenvalue problem for $\phi(X), \psi(Y)$, and $\Gamma(T)$, permitting separate treatment of space and time and reducing the two-region system to tractable modal components.

2.3.1. Eigenfunctions in the X-direction

The general solution in region I is:

$$\phi(X) = c_1\sin(\alpha X) + c_2\cos(\alpha X), 0 \le X \le L_m/L_x \tag{32}$$

and in region II:

$$\phi(X) = c_3\sin(\alpha X) + c_4\cos(\alpha X), L_m/L_x \le X \le 1. \tag{33}$$

The relationship among the unknown coefficients c_1, c_2, c_3, and c_4 is established. Furthermore, α is determined using the boundary conditions in (26)–(31). The boundary condition at $X = 0$ from (26) necessitates that:

$$c_2 = 0. \tag{34}$$

Enforcing continuity and flux conditions at $X = L_m/L_x$ and the boundary condition at $X = 1$ produces:

$$c_1\sin\left(\alpha\frac{L_m}{L_x}\right) = c_3\sin\left(\alpha\frac{L_m}{L_x}\right) + c_4\cos\left(\alpha\frac{L_m}{L_x}\right) \tag{35}$$

$$c_1\alpha\cos\left(\alpha\frac{L_m}{L_x}\right) = \frac{K_{2,x}}{K_{1,x}}\left[c_3\alpha\cos\left(\alpha\frac{L_m}{L_x}\right) - c_4\alpha\sin\left(\alpha\frac{L_m}{L_x}\right)\right] \tag{36}$$

$$c_3\alpha\cos(\alpha) - c_4\alpha\sin(\alpha) = 0. \tag{37}$$

These equations form a homogeneous linear system. A non-trivial solution requires that the determinant vanish:

$$\begin{vmatrix} A_{11} & A_{12} & A_{13} \\ A_{21} & A_{22} & A_{23} \\ 0 & A_{32} & A_{33} \end{vmatrix} = 0 \tag{38}$$

where coefficients are defined in (39)–(47):

$$A_{11} = \sin\left(\alpha \frac{L_m}{L_x}\right) \tag{39}$$

$$A_{12} = -\sin\left(\alpha \frac{L_m}{L_x}\right) \tag{40}$$

$$A_{13} = -\cos\left(\alpha \frac{L_m}{L_x}\right) \tag{41}$$

$$A_{21} = \alpha \cos\left(\alpha \frac{L_s}{L_x}\right) \tag{42}$$

$$A_{22} = -\frac{K_{2,x}}{K_{1,x}} \alpha \cos\left(\alpha \frac{L_m}{L_x}\right) \tag{43}$$

$$A_{23} = \frac{K_{2,x}}{K_{1,x}} \alpha \sin\left(\alpha \frac{L_m}{L_x}\right) \tag{44}$$

$$A_{31} = 0 \tag{45}$$

$$A_{32} = \alpha \cos(\alpha) \tag{46}$$

$$A_{33} = -\alpha \sin(\alpha). \tag{47}$$

The eigenvalues α_m are obtained as the positive roots of α in (38), and the associated eigenfunctions are denoted $\phi(X, \alpha_m) \equiv \phi_m(X)$.

2.3.2. Eigenfunctions in the Y direction

The vertical eigenfunctions are given by:

$$\psi(Y, \beta_n) \equiv \psi_n(Y) = \sin(\beta_n Y) \tag{48}$$

with $\beta_n = \frac{n\pi}{2}, n \in$ *Natural numbers*.

2.3.3. Recharge expansion and normalization

The spatial recharge distribution can be expanded in terms of the eigenfunctions:

$$R(X,Y) = \sum_{m=1}^{\infty} \sum_{n=1}^{\infty} {R_{mn}}^* \phi_m(X) \psi_n(Y) \tag{49}$$

where the modal coefficients ${R_{mn}}^*$ and normalization factors are defined in (50) and (51):

$${R_{mn}}^* = \begin{cases} \frac{1}{N} \int_0^1 \int_0^{L_m/L_x} R(X,Y) \phi_m(X)\, \psi_n(Y)\, dXdY \\ \frac{1}{N} \int_0^1 \int_{L_m/L_x}^1 R(X,Y) \phi_m(X) \psi_n(Y)\, dXdY \end{cases} \tag{50}$$

and $N(\alpha_m, \beta_n)$ is calculated as:

$$N(\alpha_m, \beta_n) = \begin{cases} \sum_m^{\infty} \sum_n^{\infty} \int_0^1 \int_0^{L_m/L_x} {\phi_m}^2(X) {\psi_n}^2(Y)\, dXdY \\ \sum_m^{\infty} \sum_n^{\infty} \int_0^1 \int_{L_m/L_x}^1 {\phi_m}^2(X) {\psi_n}^2(Y)\, dXdY \end{cases}. \quad (51)$$

2.3.4. Temporal ODE and modal dynamics

Substituting the expansions into the governing equations leads to the modal equations:

$$\Gamma\psi_n \frac{d^2\phi_m}{dX^2} + \Gamma\phi_m p_1 \frac{d^2\psi_n}{dY^2} + \phi_m\psi_n\gamma_1 \frac{1}{N} {R_{mn}}^* = \phi_m\psi_n\tau_1 \frac{d\Gamma}{dT}, 0 \le X \le L_m/L_x \quad (52)$$

$$\Gamma\psi_n \frac{d^2\phi_m}{dX^2} + \Gamma\phi_m p_2 \frac{d^2\psi_n}{dY^2} + \phi_m\psi_n\gamma_2 \frac{1}{N} {R_{mn}}^* = \phi_m\psi_n\tau_2 \frac{d\Gamma}{dT}, L_m/L_x \le X \le 1. \quad (53)$$

By substituting for the terms $\frac{d^2\phi_m(X)}{dX^2}$ and $p_1 \frac{d^2\psi_n(Y)}{dY^2}$ with $-{\alpha_m}^2\phi$ and $-{\beta_n}^2\psi$, respectively, based on the eigenvalue problems, Eqs (52) and (53) are reformulated as:

$$\frac{d\Gamma}{dT} + (\frac{1}{\tau_1}{\alpha_m}^2 + \frac{p_1}{\tau_1}{\beta_n}^2)\Gamma - \frac{\gamma_1}{\tau_1}\frac{1}{N}{R_{mn}}^* = 0, 0 \le X \le L_m/L_x \quad (54)$$

$$\frac{d\Gamma}{dT} + (\frac{1}{\tau_2}{\alpha_m}^2 + \frac{p_2}{\tau_2}{\beta_n}^2)\Gamma - \frac{\gamma_2}{\tau_2}\frac{1}{N}{R_{mn}}^* = 0, L_m/L_x \le X \le 1. \quad (55)$$

The corresponding solutions are:

$$\Gamma(T) = \frac{\gamma_1}{\tau_1}\frac{1}{N} e^{-\left(\frac{1}{\tau_1}{\alpha_m}^2 + \frac{p_1}{\tau_1}{\beta_n}^2\right)T} \int_0^T e^{(\frac{1}{\tau_1}{\alpha_m}^2 + \frac{p_1}{\tau_1}{\beta_n}^2)T'} {R_{mn}}^*\, dT', 0 \le X \le L_m/L_x \quad (56)$$

$$\Gamma(T) = \frac{\gamma_2}{\tau_2}\frac{1}{N} e^{-\left(\frac{1}{\tau_2}{\alpha_m}^2 + \frac{p_2}{\tau_2}{\beta_n}^2\right)T} \int_0^T e^{(\frac{1}{\tau_2}{\alpha_m}^2 + \frac{p_2}{\tau_2}{\beta_n}^2)T'} {R_{mn}}^*\, dT', L_m/L_x \le X \le 1. \quad (57)$$

2.3.5. Final solution for head and flux

Upon substituting the eigenfunctions $\phi_m(X)$ and $\psi_n(Y)$, and (56) and (57) into (23), the complete solution for groundwater head is:

$$H(X,Y,T) = \begin{cases} \sum_{m=1}^{\infty}\sum_{n=1}^{\infty} \frac{\gamma_1}{N}\frac{1}{{\alpha_m}^2 + p_1{\beta_n}^2}\left(1 - e^{-\left(\frac{1}{\tau_1}{\alpha_m}^2 + \frac{p_1}{\tau_1}{\beta_n}^2\right)T}\right)\phi_m(X)\psi_n(Y){R_{mn}}^* \\ \qquad , 0 \le X \le L_m/L_x \\ \sum_{m=1}^{\infty}\sum_{n=1}^{\infty} \frac{\gamma_2}{N}\frac{1}{{\alpha_m}^2 + p_2{\beta_n}^2}\left(1 - e^{-\left(\frac{1}{\tau_2}{\alpha_m}^2 + \frac{p_2}{\tau_2}{\beta_n}^2\right)T}\right)\phi_m(X)\psi_n(Y){R_{mn}}^* \\ \qquad , L_m/L_x \le X \le 1 \end{cases}. \quad (58)$$

Differentiating the head solution yields the Darcy flux in the x direction:

$$Q_x(X,Y,T) = -\begin{cases} \sum_{m=1}^{\infty}\sum_{n=1}^{\infty}\frac{\gamma_1}{N}\frac{c_1\alpha_m}{{\alpha_m}^2+p_1{\beta_n}^2}\left(1-e^{-\left(\frac{1}{\tau_1}{\alpha_m}^2+\frac{p_1}{\tau_1}{\beta_n}^2\right)T}\right)\cos(\alpha_m X)\sin(\beta_n Y){R_{mn}}^* \\ , 0 \le X \le L_m/L_x \\ \sum_{m=1}^{\infty}\sum_{n=1}^{\infty}\frac{\gamma_2}{N}\frac{\alpha_m}{{\alpha_m}^2+p_2{\beta_n}^2}\left(1-e^{-\left(\frac{1}{\tau_2}{\alpha_m}^2+\frac{p_2}{\tau_2}{\beta_n}^2\right)T}\right) \\ [c_3\cos(\alpha_m X)-c_4\sin(\alpha_m X)]\sin(\beta_n Y)\,{R_{mn}}^* \\ , L_m/L_x \le X \le 1 \end{cases} \quad (59)$$

2.4. Numerical solution to the nonlinear equation

To benchmark the linearized solution, we also advance the full nonlinear system using an explicit MacCormack predictor–corrector scheme. Each step consists of a forward-difference prediction followed by a backward-difference correction; the updated expressions for regions I and II are given in (60)–(65). This choice provides second-order accuracy and mild numerical damping that suppresses spurious oscillations without special handling of source terms.

For region I ($0 < X < L_m/L_x,\ 0 \le y \le 1$), the predictor step gives:

$$H^*_{i,j,k+1} = H_{i,j,k} + \tau_1\frac{\Delta T}{(\Delta X)^2}\left[H_{i+1,j,k}\left(H_{i+1,j,k}-H_{i,j,k}\right)-H_{i,j,k}\left(H_{i,j,k}-H_{i-1,j,k}\right)\right]+$$

$$\tau_1 p_1\frac{\Delta T}{(\Delta Y)^2}\left[H_{i,j+1,k}\left(H_{i,j+1,k}-H_{i,j,k}\right)-H_{i,j,k}\left(H_{i,j,k}-H_{i,j-1,k}\right)\right]+\tau_1\gamma_1\Delta T \quad (60)$$

$$H^*_{i,j,k+1} = H_{i,j,k} + \tau_2\frac{\Delta T}{(\Delta X)^2}\left[H_{i+1,j,k}\left(H_{i+1,j,k}-H_{i,j,k}\right)-H_{i,j,k}\left(H_{i,j,k}-H_{i-1,j,k}\right)\right]+$$

$$\tau_2 p_2\frac{\Delta T}{(\Delta Y)^2}\left[H_{i,j+1,k}\left(H_{i,j+1,k}-H_{i,j,k}\right)-H_{i,j,k}\left(H_{i,j,k}-H_{i,j-1,k}\right)\right]+\tau_2\gamma_2\Delta T. \quad (61)$$

In the corrector step, forward differences for time are retained, while backward spatial differences are used.

For region I:

$$H^{**}_{i,j,k+1} = H_{i,j,k} + \tau_1\frac{\Delta T}{(\Delta X)^2}\left[H^*_{i,j,k+1}\left(H^*_{i+1,j,k+1}-H^*_{i,j,k+1}\right)-H^*_{i-1,j,k+1}\left(H^*_{i,j,k+1}-H^*_{i-1,j,k+1}\right)\right]+$$

$$\tau_1 p_1\frac{\Delta T}{(\Delta Y)^2}\left[H^*_{i,j,k+1}\left(H^*_{i,j+1,k+1}-H^*_{i,j,k+1}\right)-H^*_{i,j-1,k+1}\left(H^*_{i,j,k+1}-H^*_{i,j-1,k+1}\right)\right]+\tau_1\gamma_1\Delta T. \quad (62)$$

For region II:

$$H^{**}_{i,j,k+1} = H_{i,j,k} + \tau_2\frac{\Delta T}{(\Delta X)^2}\left[H^*_{i,j,k+1}\left(H^*_{i+1,j,k+1}-H^*_{i,j,k+1}\right)-H^*_{i-1,j,k+1}\left(H^*_{i,j,k+1}-H^*_{i-1,j,k+1}\right)\right]+$$

$$\tau_2 p_2\frac{\Delta T}{(\Delta Y)^2}\left[H^*_{i,j,k+1}\left(H^*_{i,j+1,k+1}-H^*_{i,j,k+1}\right)-H^*_{i,j-1,k+1}\left(H^*_{i,j,k+1}-H^*_{i,j-1,k+1}\right)\right]+\tau_2\gamma_2\Delta T. \quad (63)$$

The final solution at each time step is obtained by averaging the predicted and corrected values.

For region I:

$$H_{i,j,k+1} = \frac{1}{2}\Big\{H_{i,j,k}+H^*_{i,j,k+1}+\tau_1\frac{\Delta T}{(\Delta X)^2}\left[H^*_{i,j,k+1}\left(H^*_{i+1,j,k+1}-H^*_{i,j,k+1}\right)-H^*_{i-1,j,k+1}\left(H^*_{i,j,k+1}-H^*_{i-1,j,k+1}\right)\right]+$$
$$\tau_1 p_1\frac{\Delta T}{(\Delta Y)^2}\left[H^*_{i,j,k+1}\left(H^*_{i,j+1,k+1}-H^*_{i,j,k+1}\right)-H^*_{i,j-1,k+1}\left(H^*_{i,j,k+1}-H^*_{i,j-1,k+1}\right)\right]\Big\}+\tau_1\gamma_1\Delta T. \quad (64)$$

For region II:

$$H_{i,j,k+1} = \frac{1}{2}\Big\{H_{i,j,k} + H^*_{i,j,k+1} + \tau_2 \frac{\Delta T}{(\Delta X)^2}\left[H^*_{i,j,k+1}\left(H^*_{i+1,j,k+1} - H^*_{i,j,k+1}\right) - H^*_{i-1,j,k+1}\left(H^*_{i,j,k+1} - H^*_{i-1,j,k+1}\right)\right] + \tau_2 p_2 \frac{\Delta T}{(\Delta Y)^2}\left[H^*_{i,j,k+1}\left(H^*_{i,j+1,k+1} - H^*_{i,j,k+1}\right) - H^*_{i,j-1,k+1}\left(H^*_{i,j,k+1} - H^*_{i,j-1,k+1}\right)\right]\Big\} + \tau_2 \gamma_2 \Delta T. \quad (65)$$

The MacCormack method is attractive because it provides second-order accuracy in time and space and introduces mild numerical dissipation that suppresses oscillations near sharp gradients. Another advantage is that no special adjustments are needed for source terms, which makes the approach well-suited to the recharge problems. Numerical stability is verified under the following conditions:

$$\frac{K_x}{S_y}\frac{\Delta t}{\Delta x} \leq 0.03 \quad (66)$$

$$\frac{K_y}{S_y}\frac{\Delta t}{\Delta y} \leq 0.05. \quad (67)$$

These criteria ensure stable numerical integration across discretizations of space and time. The numerical results obtained under these conditions are later compared with the analytical solutions to assess accuracy and convergence.

3. Comparison of analytical and numerical solutions

To assess the validity of the analytical formulation, results are compared with those obtained from the nonlinear finite difference simulations described in Section 2.4. The agreement between both solutions is quantified by the L2-norm (Bansal et al. [32]), which evaluates the average difference between analytical and numerical groundwater heads, H_{ana} and numerical H_{num} over $X \in [0,1]$:

$$\|H_{num} - H_{ana}\| = \left[\int_0^1 (H_{num} - H_{ana})^2 dX\right]^{1/2}. \quad (68)$$

This measure provides a convenient way to evaluate the overall agreement between the two approaches.

Figure 2 illustrates groundwater level distributions predicted by the analytical model (solid lines) and the numerical solution (symbols) under homogeneous conditions in each region. The parameters used are $S_{y,1} = 0.14, S_{y,2} = 0.26, K_{1,x} = K_{1,y} = 15\ \mathrm{m/d}, K_{2,x} = K_{2,y} = 25\ \mathrm{m/d}, r = 10\ \mathrm{mm/d}$, and $L_m = 0.5L$. Results are shown for recharge durations of 5, 10, and 15 days. The analytical and numerical profiles align closely, with the analytical solution predicting higher water levels in the less permeable region ($X < 0.5$). Computed L2 norms for these cases are 0.133, 0.144, and 0.184, confirming the small discrepancies.

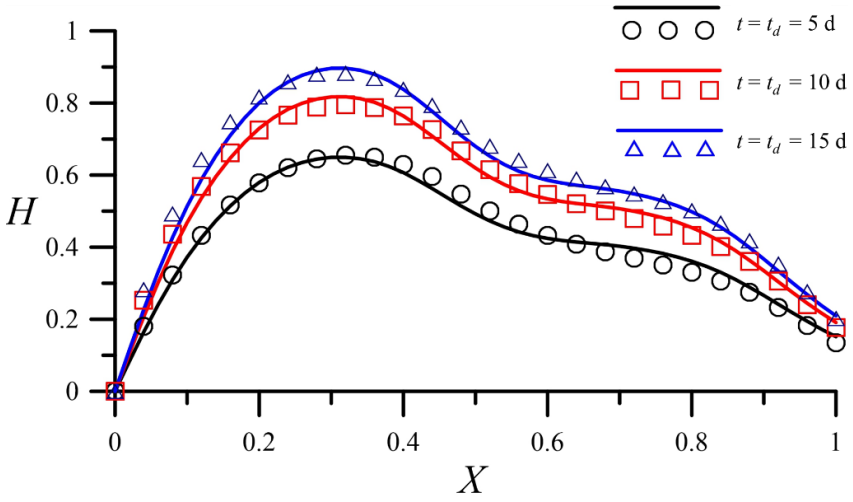

Figure 2. Comparison between analytical predictions (solid lines) and finite difference simulations (symbols) of groundwater levels at different times ($K_{1,x} = K_{1,y} = 15$ m/d, $K_{2,x} = K_{2,y} = 25$ m/d).

Figure 3 presents the results under reversed soil properties: $K_{1,x} = K_{1,y} = 25$ m/d, $K_{2,x} = K_{2,y} = 15$ m/d, $r = 10$ mm/d, with $S_{y,1} = 0.26$ and $S_{y,2} = 0.14$. Here, groundwater levels in the more permeable region ($X < 0.5$) are lower, demonstrating the inverse relationship between conductivity and water table elevation. The analytical solution again reproduces the numerical patterns, with L2-norms of 0.142, 0.179, and 0.171 for 5, 10, and 15 days, respectively.

Overall, the differences between the analytical and numerical solutions are small, with all L2-norms below 0.2. This confirms that the analytical model provides a reliable approximation to the nonlinear problem. Minor deviations can be attributed to the linearization of the governing equations and to heterogeneity effects. The findings suggest that accuracy can be further improved in numerical simulations by balancing conductivity values and storage parameters, which is consistent with the stability conditions (Eqs (66) and (67)).

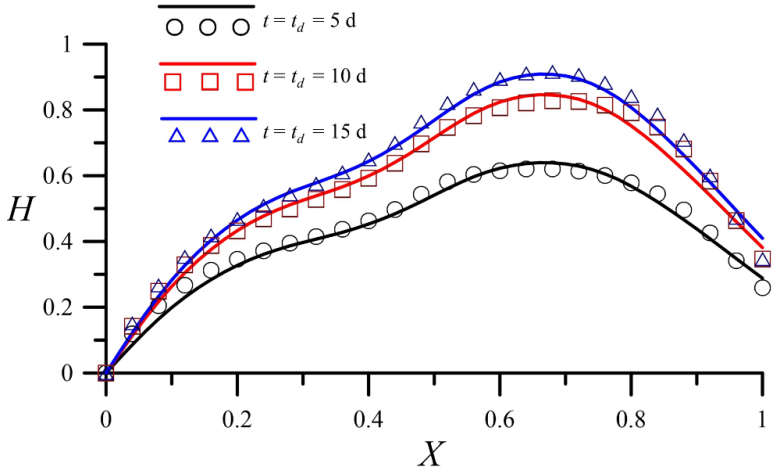

Figure 3. Analytical (solid lines) and numerical (symbols) results for groundwater levels under contrasting soil properties in regions I and II ($K_{1,x} = K_{1,y} = 25$ m/d, $K_{2,x} = K_{2,y} = 15$ m/d, $S_{y,1} = 0.26, S_{y,2} = 0.14$).

4. Discussion

The analytical solution is further analyzed to examine the effects of aquifer properties and recharge distribution on groundwater response. Figures 4–12 provide detailed comparisons and sensitivity analyses.

When using the GITT, the number of eigenvalues considerably affects the precision, accuracy, and convergence of analytical solutions. This study establishes the following criterion for solution convergence: The relative error between the sum of the leading n^{th} terms and that of the leading $(n+1)^{th}$ terms must be below 1%. Figure 4 illustrates how groundwater level changes converge with the increasing numbers of eigenvalues under two scenarios. In case (a), hydraulic conductivity is the dominant factor, with parameters $S_{y,1} = 0.1$, $S_{y,2} = 0.12$, $K_{1,x} = K_{1,y} = 1\ \mathrm{m/d}$, and $K_{2,x} = K_{2,y} = 2\ \mathrm{m/d}$. Convergence is achieved with 42 eigenvalues in the X-direction and 36 in the Y-direction. In case (b), specific yield exerts greater influence, with parameters $S_{y,1} = 0.1$, $S_{y,2} = 0.2$, $K_{1,x} = K_{1,y} = 1\ \mathrm{m/d}$, and $K_{2,x} = K_{2,y} = 1.2\ \mathrm{m/d}$. Here, 42 eigenvalues are again needed in the X-direction, while 38 are required in the Y-direction. Both scenarios confirm the rapid convergence of the analytical solution and demonstrate the robustness of the GITT approach in handling variations in aquifer properties.

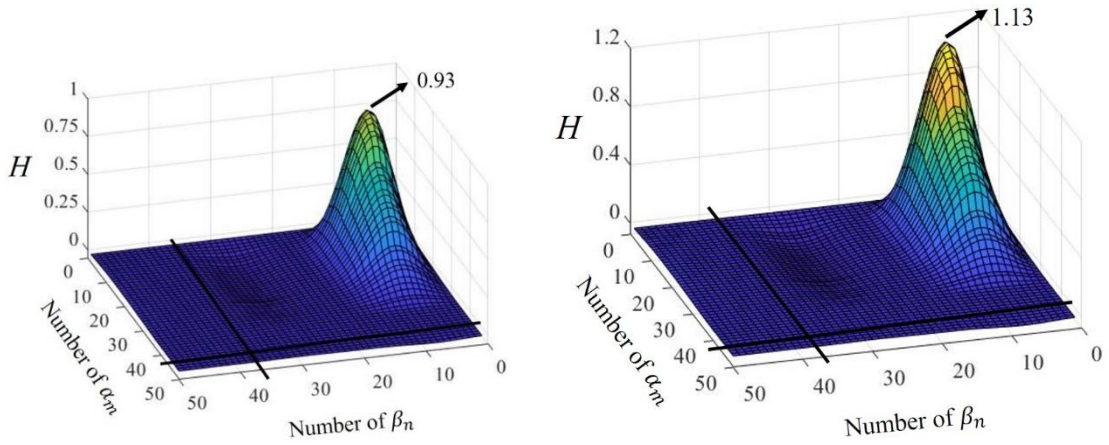

Figure 4. Convergence of the generalized integral transform solution: Number of eigenvalues required in the X and Y directions for (a) hydraulic conductivity and (b) specific yield as dominant controlling factors.

In Figure 5, we compare groundwater level responses under variations in aquifer properties and recharge. The solid black line denotes the homogeneous baseline under uniform recharge for 10 days; circle markers indicate the case with S_y increased by 50% in region II; and diamond markers indicate that K increased by 50% in region II. Relative to the baseline, boosting either S_y or K in region II lowers groundwater levels by about 5–10%. In contrast, a 50% recharge increase in region II produces much larger effects, raising the water level by ~90% in the low-permeability zone and ~20% in the high-permeability zone, underscoring the dominant influence of recharge variability.

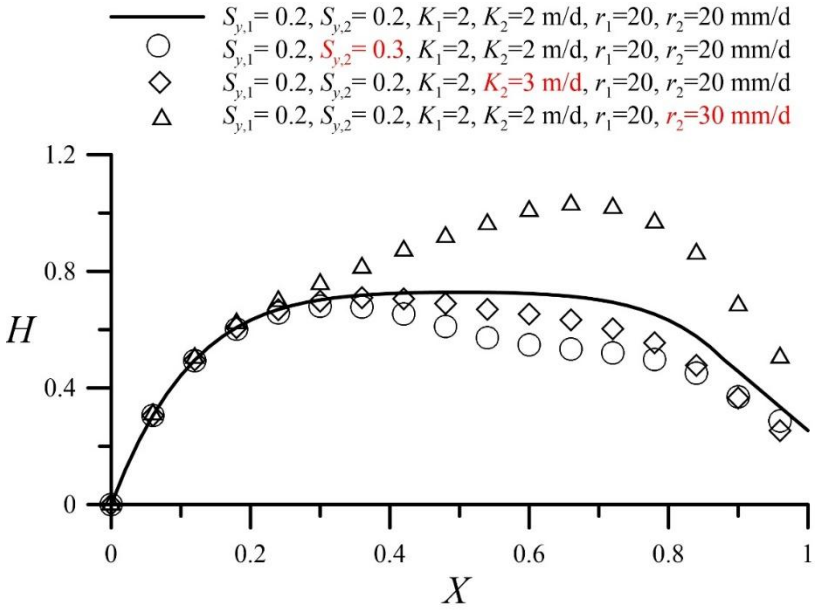

Figure 5. Spatial distributions of groundwater levels for different key parameters.

Figure 6 evaluates parameter sensitivity using a difference-ratio metric to compare the impact of specific yield, hydraulic conductivity, and recharge on the water-table response. The analysis shows a hierarchy: Recharge exerts the largest effect (maximum difference ratio 33%), followed by specific yield (19%), with hydraulic conductivity the least (11%). Physically, this ranking reflects that recharge directly perturbs the mass balance over the domain, whereas S_y and K primarily modulate storage and transmissive capacity. Thus, even moderate spatial variability in recharge can dominate head fluctuations, while comparable fractional changes in S_y or K yield smaller responses.

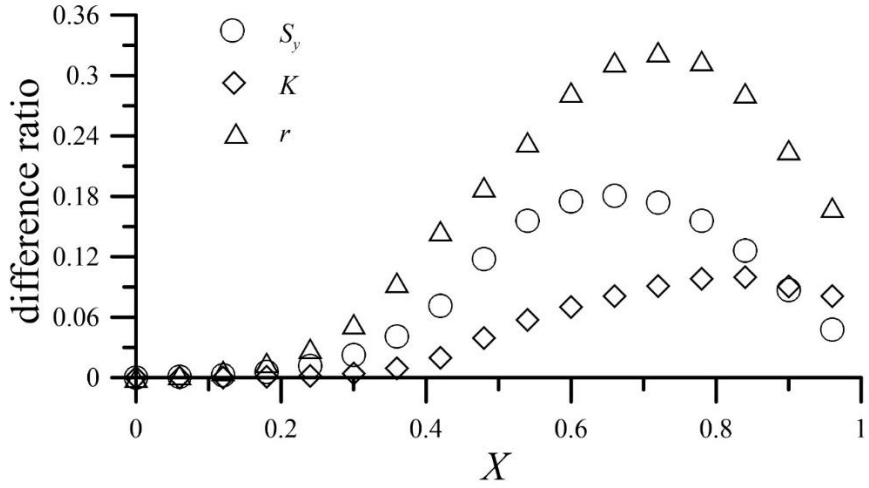

Figure 6. Sensitivity analysis expressed as difference ratios for specific yield, hydraulic conductivity, and recharge.

To demonstrate the practical interpretation of the proposed two-region (composite) aquifer framework, we present an application-style case motivated by the western Taiwan alluvial plain, particularly the Zhuoshui River basin, where low-permeability fine sediments have accumulated

within an alluvial fan and exert strong control on regional groundwater dynamics. The two zones represent a conceptual, piecewise-constant parameterization of contrasting alluvial facies (application-style illustration; not a site-calibrated model). In this setting, the subsurface commonly exhibits sharp lateral contrasts in hydraulic properties due to spatially varying depositional facies, making a two-region conceptualization a useful first-order representation for analyzing groundwater flow and redistribution under recharge forcing.

Figure 7 provides a baseline two-region scenario that reflects a common alluvial-plain condition in which a more conductive zone is hydraulically connected to a less conductive zone. Under uniform recharge, the groundwater mound develops more prominently in region II, the lower-permeability zone (Figure 7(a)). The elevated mound produces higher hydraulic gradients, which in turn accelerates flow within this region. The discharge contours in Figure 7(b) confirm this behavior: Areas of higher contour density correspond to stronger groundwater fluxes, reflecting the enhanced gradients generated by the mound.

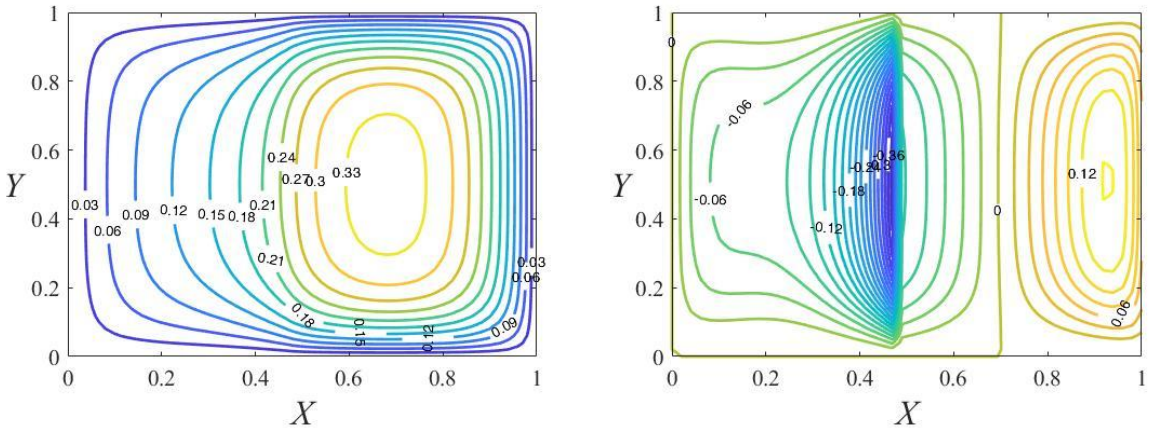

(a) Contours of water level (b) Contours of discharge Q_x

Figure 7. Zhuoshui River basin (western Taiwan) application-style two-region alluvial aquifer case under uniform recharge ($S_{y,1} = 0.3$, $S_{y,2} = 0.1$, $K_{1,x} = K_{1,y} = 4$ m/d, $K_{2,x} = K_{2,y} = 1$ m/d, $r = 25$ mm/d).

Figure 8 shows a spatially increasing recharge pattern across the two-region domain with five equal intervals under the same aquifer properties as Figure 7. In this scenario, recharge is lower in region I but progressively intensifies toward region II. Because region II has limited drainage capacity, recharge accumulates there, producing a pronounced groundwater mound (Figure 8(a)). The resulting head buildup steepens the hydraulic gradient, which drives stronger flow compared with the uniform recharge case. This effect is evident in Figure 8(b), where discharge contours are denser than those in Figure 7(b), indicating higher flow rates under the spatially increasing recharge pattern. In the context of western Taiwan alluvial deposits, this scenario serves as a proxy for cases in which recharge supply is spatially biased toward areas where fine-grained materials reduce drainage efficiency.

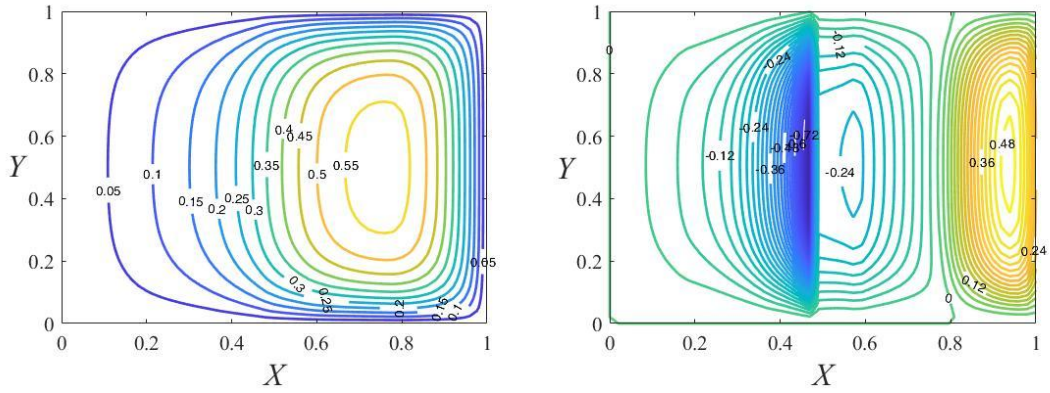

(a) Contours of water level (b) Contours of discharge Q_x

Figure 8. Zhuoshui River basin (western Taiwan) application-style two-region alluvial aquifer case: Effect of spatially increasing recharge across the two-region domain. (a) Groundwater mound development and (b) discharge Q_x contours ($S_{y,1} = 0.3, S_{y,2} = 0.1$, $K_{1,x} = K_{1,y} = 4$ m/d, $K_{2,x} = K_{2,y} = 1$ m/d, $r(x) = [10,20,30,40,50]$ mm/d).

Figure 9 shows the complementary case of spatially decreasing recharge ($r(x) = [50,40,30,20,10]$ mm/d), where recharge is highest in region I and lowest in region II. Although the geologic setting is identical to that in Figures 7–8, the head field reorganizes because the recharge pattern contrasts with the aquifer's heterogeneity. A central groundwater mound forms, from which flow spreads outward toward both boundaries (Figure 9(a)), producing a more even distribution of heads compared with the increasing-recharge case in Figure 8. Discharge contours (Figure 9(b)) confirm higher gradients and faster flow near $X = 0$, where recharge is concentrated, and gentler gradients in the downstream low-recharge zone. This result underscores a management-relevant point for alluvial systems such as the Zhuoshui River basin: Spatial recharge patterns can compete with, and in some cases outweigh, geologic asymmetry, thereby controlling mound location and drainage directionality.

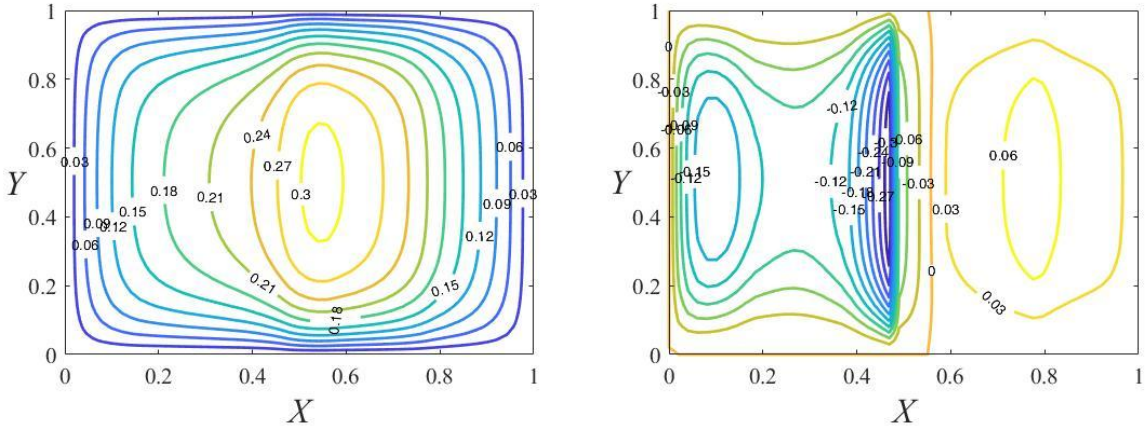

(a) Contours of water level (b) Contours of discharge Q_x

Figure 9. Zhuoshui River basin (western Taiwan) application-style two-region alluvial aquifer case: Effect of spatially decreasing recharge across the two-region domain. (a) Groundwater mound distribution and (b) discharge Q_x contours ($S_{y,1} = 0.3, S_{y,2} = 0.1$, $K_{1,x} = K_{1,y} = 4$ m/d, $K_{2,x} = K_{2,y} = 1$ m/d, $r(x) = [50,40,30,20,10]$ mm/d).

Alluvial deposits along the western Taiwan plain exhibit systematic textural changes and facies juxtapositions, motivating the use of representative soil combinations to quantify how property contrasts affect two-region responses. Figure 10 shows two application-style realizations using soil-texture proxies: (i) A moderate-contrast pairing, silty loam and sandy loam (region I: $S_y = 0.26, K_x = K_y = 2.92$ m/d; region II: $S_y = 0.34, K_x = K_y = 4.27$ m/d, $r = 10$ mm/d), and (ii) a stronger-contrast pairing, loam and sandy loam (region I: $S_y = 0.12, K_x = K_y = 1.54$ m/d; region II: $S_y = 0.34, K_x = K_y = 4.27$ m/d, $r = 10$ mm/d). The simulations show that increasing soil-property contrast amplifies both head differences and discharge transitions across the interface, producing sharper flow reorganization where materials change abruptly, an effect that is consistent with the expected behavior of composite alluvial aquifers.

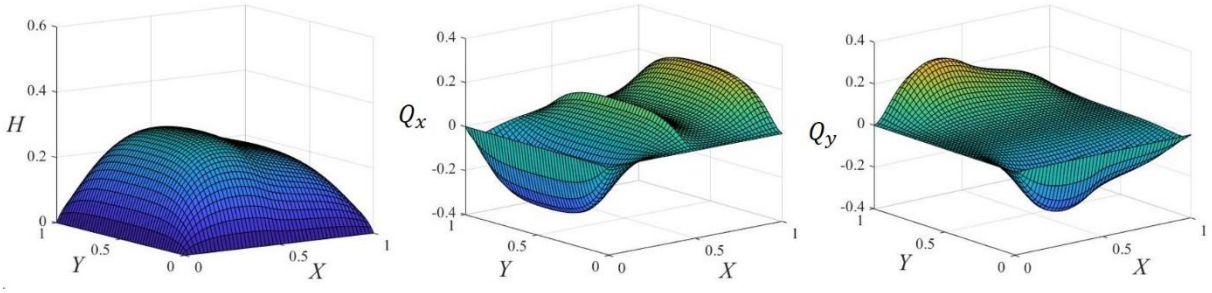

(a) region I: $S_y = 0.26, K_x = K_y = 2.92$ m/d; region II: $S_y = 0.34, K_x = K_y = 4.27$ m/d, $r = 10$ mm/d

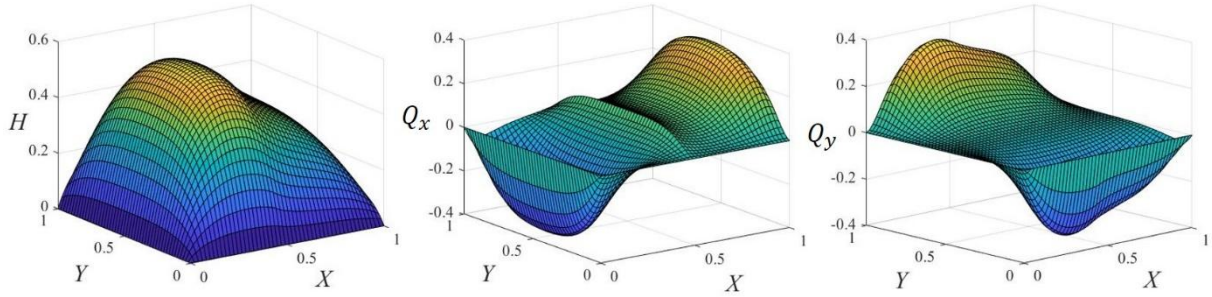

(b) region I: $S_y = 0.12, K_x = K_y = 1.54$ m/d; region II: $S_y = 0.34, K_x = K_y = 4.27$ m/d, $r = 10$ mm/d

Figure 10. Zhuoshui River basin (western Taiwan) application-style two-region alluvial aquifer case: Simulated groundwater levels and flow discharges for two representative two-region soil combinations reflecting plausible alluvial contrasts. (a) Silty loam (region I) versus sandy loam (region II); and (b) loam (region I) versus sandy loam (region II).

Soil composition and its spatial arrangement strongly modulate head and flux. In highly permeable aquifers, elevated hydraulic conductivity facilitates rapid flow, limiting water accumulation and leading to lower groundwater levels. In the first simulated case (Figure 10(a)), the aquifer consists of soils with relatively minor contrasts in properties: Region I is silty loam and region II is sandy loam, both exhibiting good permeability. Under these conditions, the groundwater level in region I is slightly higher than in region II, reflecting the lower conductivity and greater water retention capacity of silty loam. When $X < 0.5$, most of the groundwater flow in the X-direction (Q_x) is directed toward the boundary at $X = 0$, producing a negative flow. As groundwater passes from the low-permeability silty

loam into the more permeable sandy loam, the flow rate increases significantly. The maximum $|Q_x|$ in the sandy loam reaches 0.36, compared with 0.25 in the silty loam (Figure 10(a)). A similar pattern is observed for Q_y, with the sandy loam supporting higher flow rates; the maximum $|Q_y|$ is 0.36 in sandy loam and 0.23 in silty loam. As groundwater approaches the $X = 0$ boundary, flow remains relatively stable, which is consistent with the differences in permeability.

The second case (Figure 10(b)) represents a more strongly two-region aquifer, with loam in region I and sandy loam in region II. At $H = 0.56$, the groundwater level in region I is higher than in region II, reflecting the lower permeability of loam relative to sandy loam. For $X < 0.5$, most of the groundwater again flows toward the boundary at $X = 0$. In this case, however, the maximum absolute $|Q_x|$ occurs near the $X = 1$ boundary rather than at the interface, highlighting how stronger heterogeneity redistributes flow. Flow in the sandy loam exceeds that in the loam, with a sharp increase at the interface where the conductivity contrast is greatest. The maximum $|Q_x|$ reaches 0.35 in the loam and 0.32 in the sandy loam. Along the X-direction, the vertical flow component $|Q_y|$ is also higher in sandy loam, reaching 0.38, compared with 0.31 in the loam. These results demonstrate that greater contrasts in soil composition amplify differences in both head distribution and discharge, producing sharper flow transitions at material interfaces.

Finally, Figure 11 reframes the Zhuoshui alluvial analogue as a recharge-allocation problem, holding the total recharge volume constant (50 mm/day) while redistributing it spatially across two zones. In case (a), recharge is concentrated in region I, the more permeable zone. Rapid drainage in this region limits water accumulation, producing a relatively low groundwater mound ($H = 0.26$), while discharge rates increase quickly due to the steep hydraulic gradients. Maximum values reach $Q_x = 0.18$ and $Q_y = 0.27$. In case (b), recharge is concentrated in region II, which has lower permeability. Drainage here is restricted, enabling groundwater to accumulate to a higher level ($H = 0.28$). The resulting steep gradients drive larger discharges, with peak values of $Q_x = 0.38$ and $Q_y = 0.47$. Case (c) distributes recharge near the interface of the two regions. A groundwater mound forms at the interface ($H = 0.27$), and flow spreads outward into both zones. The maximum discharges are $Q_x = 0.21$ $Q_y = 0.34$ in region I and $Q_x = 0.25$ and $Q_y = 0.28$ in region II, reflecting a balanced contribution from both sides. Case (d) applies uniform recharge across the aquifer. This produces the smallest groundwater mound ($H = 0.18$) and the most even flow distribution, with maximum values of $Q_x = 0.19$ and $Q_y = 0.29$.

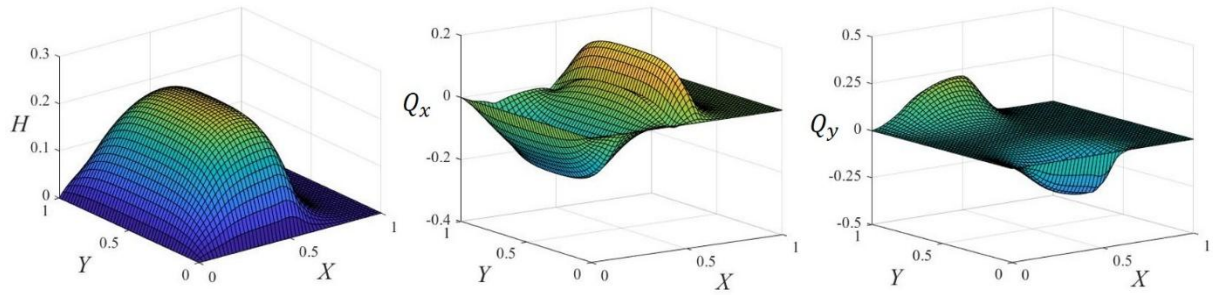

(a) $r(x) = [10,20,20,0,0]$ mm/d

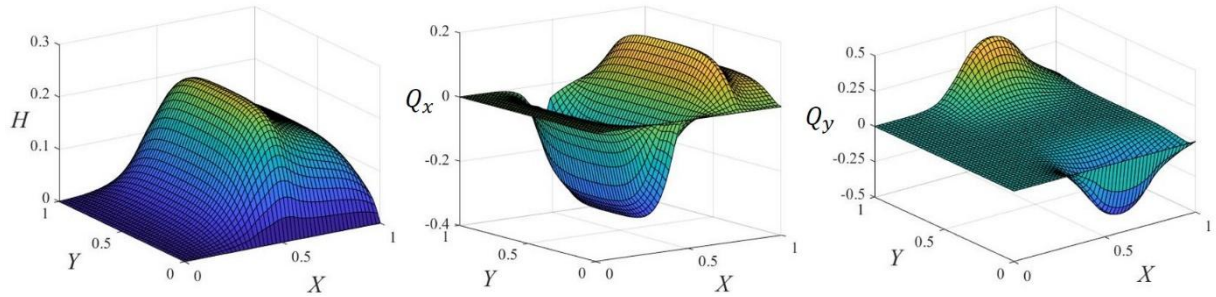

(b) $r(x) = [0,0,20,20,10]$ mm/d

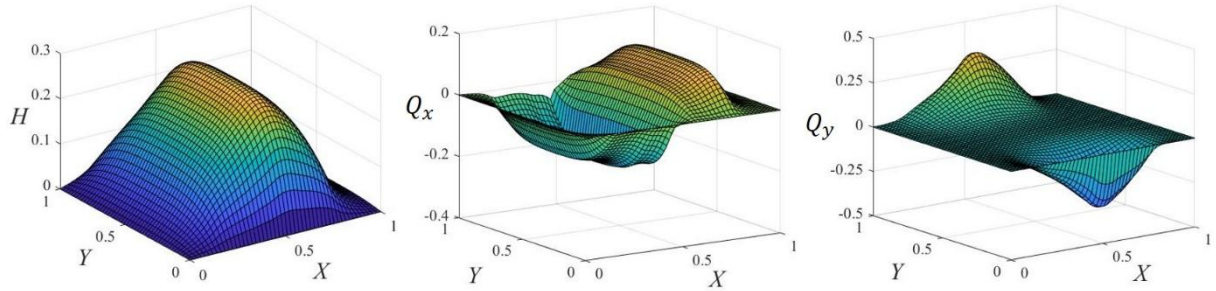

(c) $r(x) = [0,15,20,15,0]$ mm/d

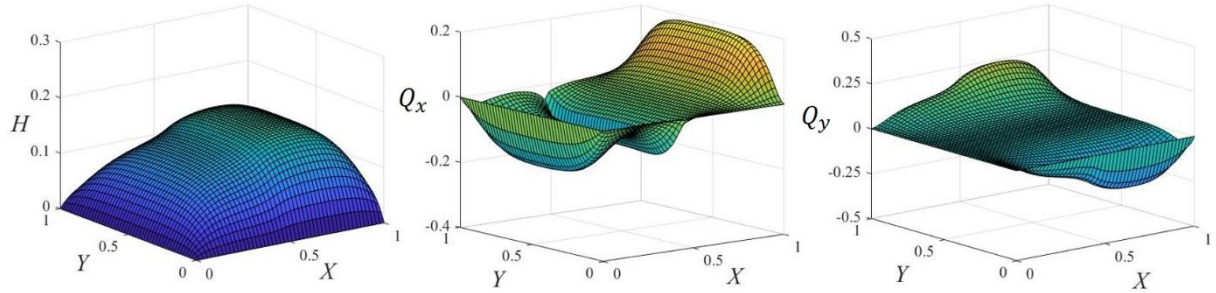

(d) $r(x) = [10,10,10,10,10]$ mm/d

Figure 11. Zhuoshui River basin (western Taiwan) application-style two-region alluvial aquifer case: Groundwater level and discharge distributions under four spatial recharge layouts with the same total daily recharge (50 mm/day) redistributed across the two zones. (a) Concentrated in region I, (b) concentrated in region II, (c) centered at the interface, and (d) uniformly distributed ($S_{y,1} = 0.34$, $S_{y,2} = 0.26$, $K_{1,x} = K_{1,y} = 4.27$ m/d, $K_{2,x} = K_{2,y} = 2.92$ m/d).

Collectively, these cases highlight a key application insight for western Taiwan alluvial systems: The spatial placement of recharge relative to permeability zoning is as influential as recharge magnitude because it directly governs whether added water is stored locally (mounding) or transmitted efficiently (drainage).

Figure 12 highlights the contrasting head–discharge behavior in homogeneous and two-region aquifers, a distinction that is critical for groundwater management and planning. In the homogeneous case, where aquifer properties are uniform, the relationship between groundwater levels and discharge is smooth and predictable. As shown in Figure 12(a), water flows steadily from the higher-head zone (Zone II) to the lower-head zone (Zone I), with gradual changes in water levels mirrored by corresponding changes in discharge. By contrast, the two-region case in Figure 12(b) reveals a more complex response caused by soil variability. At the interface between zones, abrupt shifts in head occur as groundwater moves from the lower-permeability zone (Zone II) into the higher-permeability zone (Zone I). The reduced conductivity in Zone II causes water levels to remain elevated for longer durations (e.g., $T = 0.5$), while flow accelerates upon reaching the interface. This produces a sudden drop in water level and a sharp increase in discharge. Downstream of the interface, discharge gradually decreases again as the hydraulic gradient weakens. These results demonstrate that heterogeneity introduces discontinuities in groundwater dynamics that homogeneous models cannot capture, underscoring the importance of accounting for material contrasts when predicting aquifer behavior.

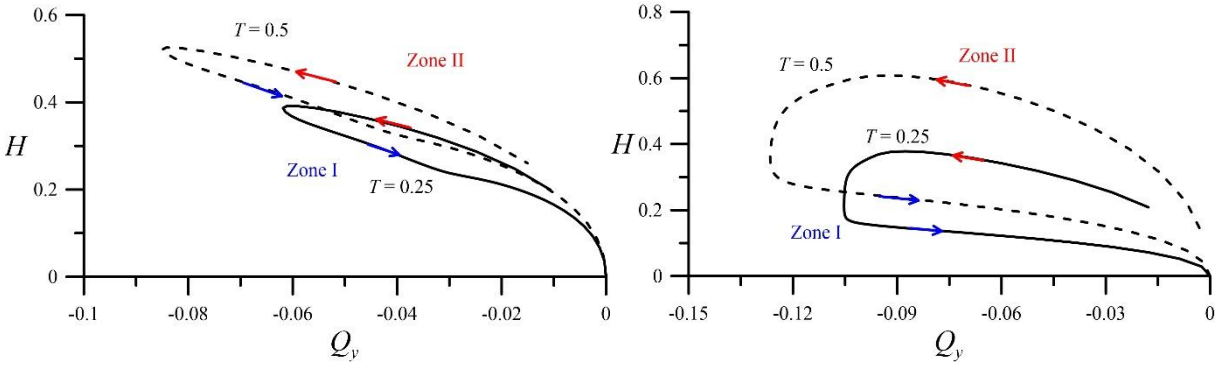

(a) Homogeneous aquifer (b) Two-region aquifer

Figure 12. Relationship between groundwater levels and discharge in (a) a homogeneous aquifer ($S_{y,1} = S_{y,2} = 0.28,\ K_{1,x} = K_{2,x} = K_{1,y} = K_{2,y} = 3.7$ m/d) and (b) a two-region aquifer ($S_{y,1} = 0.28, S_{y,2} = 0.21,\ K_{1,x} = K_{1,y} = 3.7$ m/d, $K_{2,x} = K_{2,y} = 1.9$ m/d).

5. Conclusions

In this study, we developed and validated a two-dimensional analytical solution for groundwater flow in a two-region unconfined aquifer subjected to spatially variable recharge using the GITT. Comparison with numerical solutions confirmed the accuracy of the linearized formulation, and systematic simulations revealed how heterogeneity and recharge distribution shape groundwater dynamics. The major conclusions are:

- The GITT-based analytical solution converges rapidly, requiring fewer than 40 eigenvalues for accurate results. This confirms its efficiency and suitability for a two-region groundwater problem.
- Recharge variability exerts the strongest control on groundwater levels, producing

changes up to 90% in mound height and 33% in sensitivity measures. Specific yield and hydraulic conductivity also affect flow but to a lesser degree (19% and 11%, respectively).

- Under uniform recharge, groundwater accumulates preferentially in low-permeability regions, producing higher mounds and steeper gradients that drive stronger localized flows.
- Spatially increasing recharge intensifies water buildup in low-conductivity zones, while decreasing recharge shifts the groundwater mound toward the aquifer center, with flow diverging to both boundaries. These results demonstrate that recharge patterning can override geological asymmetry in setting flow pathways.
- Contrasts in soil properties significantly alter groundwater levels and discharge. Larger differences in conductivity (e.g., loam vs. sandy loam) amplify head differences and create sharper transitions in flow across interfaces.
- The spatial allocation of recharge is as important as its total volume. Moreover, concentrating recharge in low-permeability zones elevates heads and steepens gradients, while uniform recharge minimizes mounding and stabilizes flow.
- Homogeneous aquifers display smooth, predictable head–discharge relationships, whereas two-region aquifers exhibit abrupt head drops and sharp flow increases at interfaces. Such discontinuities highlight the need to account for material contrasts in groundwater modeling.

Overall, the results emphasize that aquifer heterogeneity and recharge distribution jointly determine groundwater response. The analytical framework developed here provides a robust tool for predicting groundwater mounding, validating numerical models, and supporting sustainable water resource management in a two-region aquifer system.

Author contributions

Ming-Chang Wu: Writing–original draft, writing–validation, methodology, investigation, formal analysis; Ping-Cheng Hsieh: Writing–review and editing, methodology, investigation, conceptualization, resources, funding acquisition. All authors have read and approved the final version of the manuscript for publication.

Use of Generative-AI tools declaration

While preparing this work, the authors used Chat-GPT and Grammarly for English editing to improve language and readability. After using this tool/service, the authors reviewed and edited the content as needed, taking full responsibility for the publication's content.

Acknowledgments

The National Science and Technology Council of Taiwan financially supported this study under Grant No. MOST 110-2313-B-005-035.

Conflict of interest

The authors declare no competing interests.

References

1. F. A. Montalto, J. Y. Parlange, T. S. Steenhuis, A simple model for predicting water table fluctuations in a tidal marsh, *Water Res. Res.,* **43** (2007), W03424. https://doi.org/10.1029/2004WR003913
2. H. Li, J. J. Jiao, Z. Tang, Semi-numerical simulation of groundwater flow induced by periodic forcing with a case-study at an island aquifer, *J. Hydrol.,* **327** (2006), 438–446. https://doi.org/10.1016/j.jhydrol.2005.11.032
3. H. Li, G. Li, J. Cheng, M. C. Boufadel, Tide-induced head fluctuations in a confined aquifer with sediment covering its outlet at the sea floor, *Water Res. Res.,* **4** (2007), W03403. https://doi.org/10.1029/2005WR004724
4. Y. Q. Xia, H. L. Li, A combined field and modeling study of groundwater flow in a tidal marsh, *Hydrol. Earth Sys. Sci.,* **16** (2012), 741–759. https://doi.org/10.5194/hess-16-741-2012
5. P. Kreyns, X. Geng, H. A. Michael, The influence of connected heterogeneity on groundwater flow and salinity distributions in coastal volcanic aquifers, *J. Hydrol.,* **586** (2020), 124863. https://doi.org/10.1016/j.jhydrol.2020.124863
6. C. L. Winter, D. M. Tartakovsky, Groundwater flow in heterogeneous composite aquifers, *Water Res. Res.,* **38** (2002), 23-1–23-12. https://doi.org/10.1029/2001WR000450
7. E. Kalbus, C. Schmidt, J. W. Molson, F. Reinstorf, M. Schirmer, Influence of aquifer and streambed heterogeneity on the distribution of groundwater discharge, *Hydrol. Earth Sys. Sci.,* **13** (2009), 69–77. https://doi.org/10.5194/hess-13-69-2009
8. W. A. Illman, J. Zhu, A. J. Craig, D. Yin, Comparison of aquifer characterization approaches through steady state groundwater model validation: A controlled laboratory sandbox study, *Water Res. Res.*, **46** (2010), W04502. https://doi.org/10.1029/2009WR007745
9. A. Hartmann, T. Gleeson, Y. Wada, T. Wagener, Enhanced groundwater recharge rates and altered recharge sensitivity to climate variability through subsurface heterogeneity, *Pro. N. Aca. Sci.*, **114** (2017), 2842–2847. https://doi.org/10.1073/pnas.1614941114
10. S. E. Serrano, Analytical solutions of the nonlinear groundwater flow equation in unconfined aquifers and the effect of heterogeneity, *Water Res. Res.,* **31** (1995), 2733–2742. https://doi.org/10.1029/95WR02038
11. M. G. Trefry, Periodic forcing in composite aquifers, *Adv. Water Res.,* **22** (1999), 645–656. https://doi.org/10.1016/S0309-1708(98)00037-2
12. M. H. Chuang, C. S. Huang, G. H. Li, H. D. Yeh, Groundwater fluctuations in heterogeneous coastal leaky aquifer systems, *Hydrol. Earth Sys. Sci.,* **14** (2010), 1819–1826. https://doi.org/10.5194/hess-14-1819-2010
13. T. Ptak, M. Piepenbrink, E. Martac, Tracer tests for the investigation of heterogeneous porous media and stochastic modelling of flow and transport—a review of some recent developments, *J. hydrol.,* **294** (2004), 122–163. https://doi.org/10.1016/j.jhydrol.2004.01.020
14. M. C. Wu, P. C. Hsieh, Improved solutions to the linearized Boussinesq equation with temporally varied rainfall recharge for a sloping aquifer, *Water,* **11** (2019), 826. https://doi.org/10.3390/w11040826
15. P. M. Morse, H. Feshbach, Methods of theoretical physics, *Am. J. Phy.,* **22** (1954), 410–413. https://doi.org/10.1119/1.1933765
16. M. N. Özisik, *Boundary value problems of heat conduction*, New York, NY, USA: Dover Publications Inc., 1968.

17. G. P. Mulholland, M. H. Cobble, Diffusion through composite media, *Inter. J. Heat Mass Trans.,* **15** (1972), 147–160. https://doi.org/10.1016/0017-9310(72)90172-X
18. Y. Sun, I. S. Wichman, On transient heat conduction in a one-dimensional composite slab, *Inter. J. Heat Mass Trans.,* **47** (2004), 1555–1559. https://doi.org/10.1016/j.ijheatmasstransfer.2003.09.011
19. Y. Zhang, Nonlinear inversion of an unconfined aquifer: Simultaneous estimation of heterogeneous hydraulic conductivities, recharge rates, and boundary conditions, *Trans. Por. Med*., **102** (2014), 275–299. https://doi.org/10.1007/s11242-014-0275-x
20. S. K. Das, S. J. Ganesh, T. S. Lundström, Modeling of a groundwater mound in a two-dimensional heterogeneous unconfined aquifer in response to precipitation recharge, *J. Hydrol. Eng.,* **20** (2015), 04014081. https://doi.org/10.1061/(ASCE)HE.1943-5584.0001071
21. J. F. Águila, J. Samper, B. Pisani, Parametric and numerical analysis of the estimation of groundwater recharge from water-table fluctuations in heterogeneous unconfined aquifers, *Hydrogeo. J.,* **27** (2019), 1309–1328. https://doi.org/10.1007/s10040-018-1908-x
22. K. Hemker, M. Bakker, Analytical solutions for whirling groundwater flow in two-dimensional heterogeneous anisotropic aquifers, *Water Resour. Res.,* **42** (2006), W12419. https://doi.org/10.1029/2006WR004901
23. H. Guo, J. J. Jiao, H. Li, Groundwater response to tidal fluctuation in a two-zone aquifer, *J. Hydrol.,* **381** (2010), 364–371. https://doi.org/10.1016/j.jhydrol.2009.12.009
24. X. Liang, Y. K. Zhang, Analytic solutions to transient groundwater flow under time-dependent sources in a heterogeneous aquifer bounded by fluctuating river stage, *Adv. Water Resour.,* **58** (2013), 1–9. https://doi.org/10.1016/j.advwatres.2013.03.010
25. M. C. Wu, P. C. Hsieh, Variation of groundwater flow caused by any spatiotemporally varied recharge, *Water,* **12** (2020), 287. https://doi.org/10.3390/w12010287
26. P. C. Hsieh, M. C. Wu, Changes in groundwater flow in an unconfined aquifer adjacent to a river under surface recharge, *Hydro. Sci. J.,* **68** (2023), 920–937. https://doi.org/10.1080/02626667.2023.2193295
27. J. Bear, *Dynamics of fluids in porous media*, New York, NY, USA: Elsevier, 1975.
28. W. Guo, Transient groundwater flow between reservoirs and water-table aquifers, *J. Hydrol.,* **195** (1997), 370–384. https://doi.org/10.1016/S0022-1694(96)03200-3
29. X. Liang, Y. K. Zhang, A new analytical method for groundwater recharge and discharge estimation, *J. Hydrol.,* **450 (**2012), 17–24. https://doi.org/10.1016/j.jhydrol.2012.05.036
30. X. Liang, Y. K. Zhang, Temporal and spatial variation and scaling of groundwater levels in a bounded unconfined aquifer, *J. Hydrol.,* **479** (2013), 139–145. https://doi.org/10.1016/j.jhydrol.2012.11.044
31. G. Gao, H. Zhan, S. Feng, B. Fu, G. Huang, A mobile–immobile model with an asymptotic scale-dependent dispersion function, *J. Hydrol.,* **424-425** (2012), 172–183. https://doi.org/10.1016/j.jhydrol.2011.12.041
32. R. K. Bansal, C. K. Lande, A. Warke, Unsteady groundwater flow over sloping beds: Analytical quantification of stream–aquifer interaction in presence of thin vertical clogging layer, *J. Hydrol. Eng.,* **21** (2016), 04016017. https://doi.org/10.1061/(ASCE)HE.1943-5584.0001362